Panchromatic small-molecule organic solar cells based on a pyrrolopyrrole aza-BODIPY with a small energy loss

Feng, Ru
Department of Applied Chemistry, Graduate School of Engineering, Kyushu University

Mori, Tatsuya
Department of Applied Chemistry, Graduate School of Engineering, Kyushu University

Yasuda, Takuma
Department of Applied Chemistry, Graduate School of Engineering, Kyushu University

Furuta, Hiroyuki
Department of Applied Chemistry, Graduate School of Engineering, Kyushu University

他

出版情報：Dyes and Pigments. 210, pp.111020-, 2023-02. Elsevier
バージョン：
権利関係：

Panchromatic small-molecule organic solar cells based on a pyrrolopyrrole aza-BODIPY with a small energy loss

Ru Feng[a, b, *], Tatsuya Mori[a, c], Takuma Yasuda[a, c], Hiroyuki Furuta[a, d], Soji Shimizu[a, d, **]

[a] *Department of Applied Chemistry, Graduate School of Engineering, Kyushu University, Fukuoka 819-0395, Japan*

[b] *School of Chemistry and Chemical Engineering, Jiangsu University, Zhenjiang 212013, PR China*

[c] *INAMORI Frontier Research Center (IFRC), Kyushu University, Fukuoka 819-0395, Japan*

[d] *Center for Molecular Systems (CMS), Kyushu University, Fukuoka 819-0395, Japan*

ABSTRACT: A small photon energy loss (E_{loss}) is one of the requisites for achieving near-infrared (NIR) small-molecule organic solar cells (SM-OSCs). Herein, we present two novel pyrrolopyrrole aza-BODIPY (PPAB)-based panchromatic chromophores, **TT-2PPAB** and **DFBT-2PPAB**, with an acceptor-donor-acceptor configuration for photovoltaic studies. Among them, in combination with [6,6]-phenyl-C_{71} butyric acid methyl ester ($PC_{71}BM$) acceptor, **TT-2PPAB** exhibits a moderate power conversion efficiency (PCE) of 3.11% due to an E_{loss} of 0.48 eV, which is smaller than the empirical limit of 0.6 eV. Based on the electrochemistry and theoretical calculations, we revealed that the efficient photovoltaic performance of the **TT-2PPAB**-based device can be ascribed to the sufficiently deep LUMO level of **TT-2PPAB** for charge transfer to $PC_{71}BM$.

1. Introduction

The advantageous characteristics of organic solar cells (OSCs), such as light weight, flexibility, solution processability, and low cost, make them a promising renewable energy source [1,2]. The development of small-molecule OSCs (SM-OSCs) has drawn increasing attention over the past decades because of their well-defined structures and high reproducibility of device performances compared with polymer solar cells (PSCs) [3–7]. Although a large number of conjugated small molecules have been developed for OSCs, the photovoltaic performance of SM-OSCs is constrained by their comparatively narrow ranges of light absorption in the visible region, in other words, large band gaps (E_g), due to the small π-conjugated systems [8,9]. Therefore, much effort has been devoted to creating panchromatic chromophores by extension of the π-conjugated systems and introduction of the donor (D)–acceptor (A) interactions. The photon energy loss (E_{loss}) defined by $E_g - eV_{oc}$, where e and V_{oc} denote the elementary charge and open-circuit voltage, respectively, is another critical factor to give an impact on the photovoltaic performance of SM-OSCs [10,11]. Compared with the E_{loss} values of perovskite solar cells (ca. 0.5 eV) and inorganic solar cells (0.3–0.6 eV), those of conventional SM-OSCs typically range from 0.6 to 1.0 eV [12]. The relatively larger E_{loss} becomes a drawback of panchromatic SM-OSCs especially when the absorption reaches the near-infrared (NIR) region. Although there have been reports on highly efficient PSCs with E_{loss} values less than 0.6 eV [10], to the best of our knowledge, SM-OSCs with such a small E_{loss} have been rather occasionally reported [13,14].

Recently, we have developed novel aza-BODIPY-based chromophores called pyrrolopyrrole aza-BODIPYs (PPABs), which exhibit far-red/NIR absorption and fluorescence with high quantum

yields because of their extended dimeric aza-BODIPY structures [15–18]. Owing to their exceptionally prominent optical properties, PPABs have been functionalized for bioimaging, sensors, and therapeutics to achieve various applications such as aggregation-induced emission enhancement (AIEE) [19,20], two-photon absorption (TPA) [21], photoacoustic imaging [22], cancer therapy [23], amine detection [20,24–29], and electrogenerated chemiluminescence (ECL) [30].

With the far-red/NIR PPAB chromophores in hand, a photovoltaic performance of SM-OSCs fabricated using PPABs and [6,6]-phenyl-C_{71} butyric acid methyl ester ($PC_{71}BM$) as p- and n-type materials was investigated in our previous study. However, due to their narrow absorption, the power conversion efficiency (PCE) was unexpectedly low [17]. A bithienyl-linked PPAB dimer was then synthesized to broaden the absorption. Despite the panchromatic absorption across the visible (vis)/NIR regions, the dimer exhibited a rather poor PCE of 0.74% due to the low solubility [31]. To improve the light absorption as well as the OSC device performance, D–A architectures using PPAB and cyclopentadithiophene (**CPDT**) as acceptor and donor units were examined (Chart 1) [32]. PPAB-CPDT triad (**CPDT-2PPAB**) and copolymer thus fabricated exhibited moderately high PCE up to 3.88% and 2.27%, respectively, despite their NIR absorption reaching over 1000 nm. The fact that the E_{loss} for **CPDT-2PPAB** (0.54 eV) and the PPAB-CPDT copolymer (0.53 eV) was lower than the empirical lower limit of 0.6 eV indicates their high compatibility with $PC_{71}BM$ owing to the sufficiently deep LUMO levels for charge transfer [32,33]. Meanwhile, there is still room for improving the V_{oc} by changing the donor units, which dominantly determine the HOMO energy levels of the triad and copolymer. As illustrated in Chart 1, we designed two novel PPAB-based A–D–A triads with thieno[*3*,*2*-*b*]thiophene (**TT-2PPAB**) and 3,3-difluoro-2,2-bithiophene (**DFBT-2PPAB**) as a donor unit for SM-OSCs with a small E_{loss} and high V_{oc}. **TT-2PPAB** in combination with $PC_{71}BM$ exhibited a moderate PCE of 3.11% with a significantly small E_{loss} value of 0.48 eV and a high V_{oc} value of 0.75 V, while **DFBT-2PPAB**-based SM-OSC showed a relatively low PCE of 1.35% due to the poor solubility of **DFBT-2PPAB**.

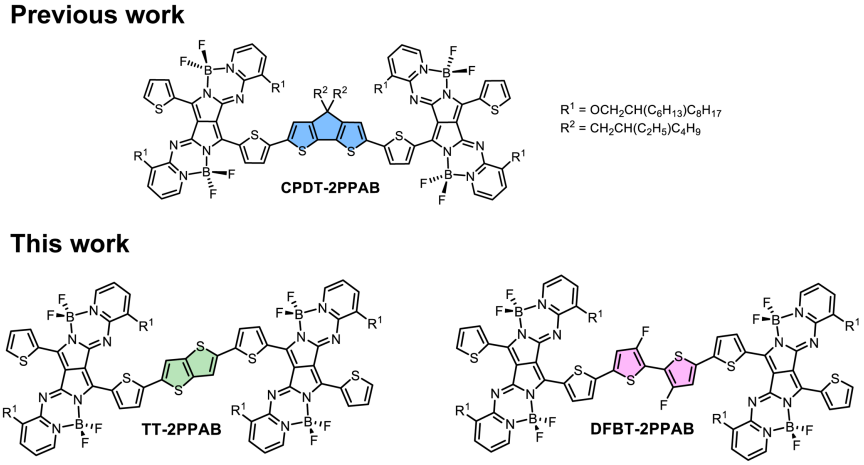

Chart 1. PPAB-based triads, **CPDT-2PPAB** in the previous work and **TT-2PPAB** and **DFBT-2PPAB** in this work.

2. Experimental

2.1 Instrumentation and measurements

Electronic absorption spectra were recorded on a JASCO V-770 spectrophotometer. Fluorescence spectra were recorded on a SPEX Fluorolog-3-NIR spectrometer (HORIBA) with a

NIR-PMT R5509 photomultiplier tube (Hamamatsu). Absolute fluorescence quantum yields were measured using a Hamamatsu Photonics C9920-03G calibrated integrating sphere system. ^{1}H and ^{19}F NMR spectra were recorded on a JEOL JNM-ECX500 spectrometer (operating at 495.132 MHz for ^{1}H and 465.889 MHz for ^{19}F) using a residual solvent as an internal reference for ^{1}H (δ = 5.32 ppm for CD_2Cl_2 and δ = 7.26 ppm for $CDCl_3$) and trifluoroacetic acid as an external reference for ^{19}F (δ = –76.55 ppm). High-resolution mass spectrometry was performed on a JEOL LMS-HX-110 spectrometer (FAB mode with 3-nitrobenzyl alcohol (NBA) as the matrix). Cyclic voltammograms and differential pulse voltammograms were recorded on a CH Instrument Model 620B (ALS) under an argon atmosphere in dichloromethane solution with 0.1 M tetra-*n*-butylammonium hexafluorophosphate (nBu$_4$N·PF$_6$) as a supporting electrolyte. Measurements were made with a glassy carbon electrode, an Ag/AgCl reference electrode, and a Pt-wire counter electrode. The concentration of the solution was fixed at 0.5 mM, and the sweep rates were set to 100 mV s^{-1}. The ferrocenium/ferrocene (Fc^+/Fc) couple was used as an internal standard. Thin-layer chromatography (TLC) was carried out on aluminum sheets coated with silica gel 60 F_{254} (MERCK). Preparative separations were performed using silica gel column chromatography (KANTO Silica Gel 60 N, spherical, neutral, 40–50 μm). All reagents and solvents used for reactions were of commercial reagent grade and were used without further purification unless noted otherwise. All solvents used in optical measurements were of commercial spectroscopic grade.

2.2 OSCs fabrication and evaluation

Prepatterned ITO-coated glass substrates were ultrasonic cleaned sequentially in detergent solution (15 min), deionized water (10 min × 2), and acetone (10 min), kept in isopropyl alcohol overnight, and then subjected to UV/ozone treatment for 30 min. A thin layer (~30 nm) of ZnO was prepared by spin-coating (at 5000 rpm for 30 s) a precursor solution of zinc acetate (1.00 g) and ethanolamine (0.28 g) in 2-methoxyethanol (10 mL) through a 0.45 μm polyethylene membrane filter, followed by baking at 200 °C for 10 min under air. The photoactive layer was then deposited by spin-coating from a chloroform solution containing a donor (5 mg mL^{-1} or 7 mg mL^{-1}) and $PC_{71}BM$ (10 mg mL^{-1} or 7 mg mL^{-1}) after passing through a 0.45 μm poly(tetrafluoroethylene) membrane filter. The thickness of the photoactive layer was ca. 39−121 nm, measured with a profilometer. The thin films were then loaded into an E-200 vacuum evaporation system (ALS Technology). Finally, 10-nm-thick MoO_3 and 100-nm-thick Ag layers were sequentially vacuum-deposited on top of the photoactive layer under a high vacuum (<5.0 × 10^{-4} Pa) through a shadow mask, defining an active area of 0.04 cm^2 for each device. The current density–voltage (J–V) characteristics and EQE spectra of the fabricated OSCs were measured with a computer-controlled Keithley 2400 source measure unit in the air, under simulated AM 1.5G solar illumination at 100 mW cm^{-2} (1 sun) conditions, using a Xe lamp-based SRO-25GD solar simulator and IPCE measurement system (Bunko Keiki). The light intensity was calibrated using a certified silicon photovoltaic reference cell.

2.3 Computational methods

The Gaussian16 [34] software package was used to carry out DFT and TDDFT calculations using the CAM-B3LYP functional with the 6-31G(d) basis set. Structural optimizations were performed on model compounds, in which alkoxy substituents were replaced with methoxy groups for simplicity.

*2.4 Synthesis of **TT-2PPAB** and **DFBT-2PPAB***

The synthesis of three precursors, **PPAB-Br** [31], **TT-2SnMe$_3$** [35], and **DFBT-2SnMe$_3$** [36] (Scheme S1), and the Stille cross coupling reactions [37] were performed according to the literature procedures.

TT-2PPAB: **PPAB-Br** (88.5 mg, 0.08 mmol), **TT-2SnMe$_3$** (18.7 mg, 0.04 mmol), and $Pd(PPh_3)_4$ (4.6 mg, 0.1 eq) were dissolved in dry toluene (6 mL). After degassing three times by freeze–pump–thaw cycles, the mixture was stirred for 16 h at 120 °C. Then, the solvent was removed in a vacuo. The crude product was dissolved in dichloromethane, and the mixture was filtered to remove the deactivated palladium reagent. The crude residue was purified by gel permeation chromatography (Bio-Beads® S-X1; eluent: CH_2Cl_2), silica gel column chromatography (eluent: hexane/ethyl acetate = 1:3 (v/v)), and recrystallized from $CHCl_3$ and hexane to give **TT-2PPAB** (58 mg, 66%) as a dark solid. HR-MS (FAB): *m/z* $[M]^+$ calcd for $C_{118}H_{156}B_4F_8N_{12}O_4S_6$, 2193.0923; found, 2193.0941. ^{1}H NMR (495 MHz, CD_2Cl_2, 298 K): δ 9.96 (d, J = 4.0 Hz, 2H), 9.41 (d, J = 3.5 Hz, 2H), 7.99 (d, J = 6.5 Hz, 2H), 7.94 (d, J = 6.0 Hz, 2H), 7.77 (d, J = 5.0 Hz, 2H), 7.60 (s, 2H), 7.44 (d, J = 4.0 Hz, 2H), 7.38–7.30 (m, 6H), 7.19–7.12 (m, 4H), 4.07–4.05 (t, J = 5.0 Hz, 8H), 2.12–2.04 (m, 8H), 1.60–1.55 (m, 16H), 1.38–1.18 (m, 80H), 0.87–0.79 (m, 24H). ^{19}F NMR (466 MHz, CD_2Cl_2, 298 K): δ –127.66 (4F), –129.16 (4F). UV/vis/NIR ($CHCl_3$): λ_{max} nm (ε mol^{-1}dm^{3}cm^{-1}): 309 (51000), 410 (56000), 482 (46000), 581 (43000), 777(106000). m.p.: 268 ºC.

DFBT-2PPAB: **DFBT-2PPAB** was synthesized in the same manner to **TT-2PPAB**. **PPAB-Br** (28.8 mg, 0.026 mmol), **DFBT-2SnMe$_3$** (7.0 mg, 0.013 mmol), and $Pd(PPh_3)_4$ (1.5 mg, 0.1 eq) were used as the starting materials. The reaction mixture was purified by gel permeation chromatography (Bio-Beads® S-X1; eluent: CH_2Cl_2). The crude product was dissolved in $CHCl_3$ and filtered. Because the impurities (PPAB dimer (purple fraction)) could be dissolved in $CHCl_3$, **DFBT-2PPAB** was collected as a dark solid. After repeating this step several times, **DFBT-2PPAB** was obtained in a pure form as a dark solid (20 mg, 69%). HR-MS (FAB): *m/z* $[M]^+$ calcd for $C_{120}H_{156}B_4F_{10}N_{12}O_4S_6$, 2255.0923; found, 2255.0909. ^{1}H NMR (495 MHz, CD_2Cl_2, 298 K): δ 9.87 (d, J = 3.5 Hz, 2H), 9.37 (d, J = 3.0 Hz, 2H), 7.98 (d, J = 6.0 Hz, 2H), 7.93 (d, J = 7.5 Hz, 2H), 7.77 (d, J = 5.0 Hz, 2H), 7.41–7.31 (m, 8H), 7.23–7.13 (m, 6H), 4.07–4.05 (t, J = 5.5 Hz, 8H), 2.10–2.04 (m, 8H), 1.58–1.52 (m, 16H), 1.39–1.19 (m, 80H), 0.87–0.80 (m, 24H). ^{19}F NMR (466 MHz, CD_2Cl_2, 298 K): δ –123.18 (2F), –127.56 (4F), –128.93 (4F). UV/vis/NIR ($CHCl_3$): λ_{max} nm (ε mol^{-1}dm^{3}cm^{-1}): 309 (51000), 410 (56000), 482 (46000), 571 (39000), 752 (110000). m.p.: 248 ºC.

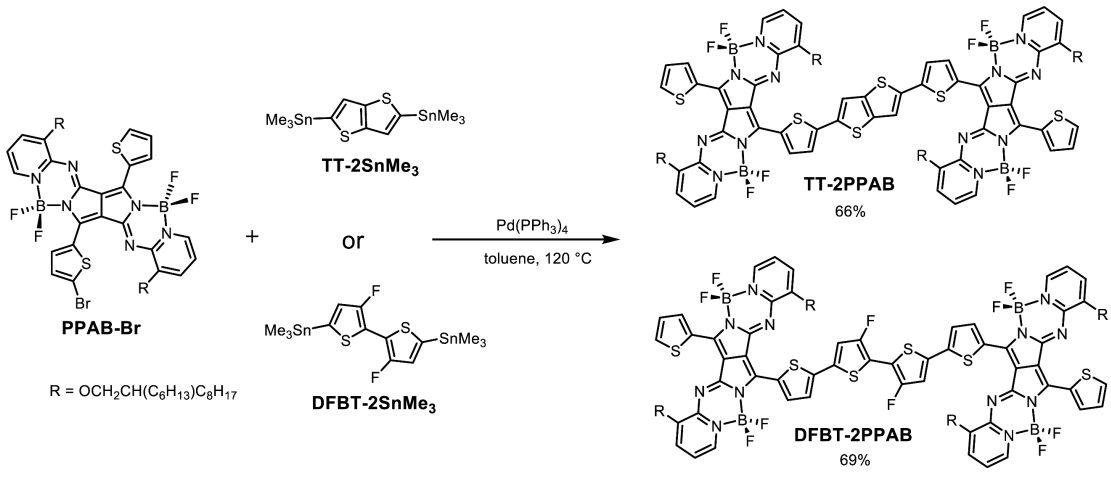

Scheme 1. Synthesis of **TT-2PPAB** and **DFBT-2PPAB**.

3. Results and discussion

3.1 Optical properties

The UV/vis/NIR absorption spectra of **TT-2PPAB** and **DFBT-2PPAB** in chloroform and the thin film state are shown in Fig. 1, and the detailed data is summarized in Table 1. Both **TT-2PPAB** and **DFBT-2PPAB** exhibit absorption from 300 nm to 850 nm with an absorption maxima at 777 and 752 nm, respectively. Due to the formation of π-stacked aggregates, their absorption maxima in the film state show red-shifts by 965 and 1090 cm^{-1} from those in solutions. Considering the smaller red-shift of 258 cm^{-1} for **CPDT-2PPAB** with bulky 2-ethylhexyl groups on the CPDT moiety in our previous study [32], the absorption spectra and degrees of aggregation of PPAB-based triads can be controlled by the donor units. The molar absorption coefficients were calculated to be 1.06×10^5 $M^{-1}cm^{-1}$ and 1.10×10^5 $M^{-1}cm^{-1}$for **TT-2PPAB** and **DFBT-2PPAB** in chloroform solution, respectively. The large molar absorption coefficients can help OSC devices to collect solar photons more efficiently, resulting in high J_{sc} values. The optical band gaps of **TT-2PPAB** and **DFBT-2PPAB** were estimated from the onset of the film absorption to be 1.35 and 1.38 eV, respectively. The fluorescence of **TT-2PPAB** and **DFBT-2PPAB** was nearly quenched (Φ_F = ~0.03), exhibiting single emission bands at 826 and 798 nm (Fig. 2).

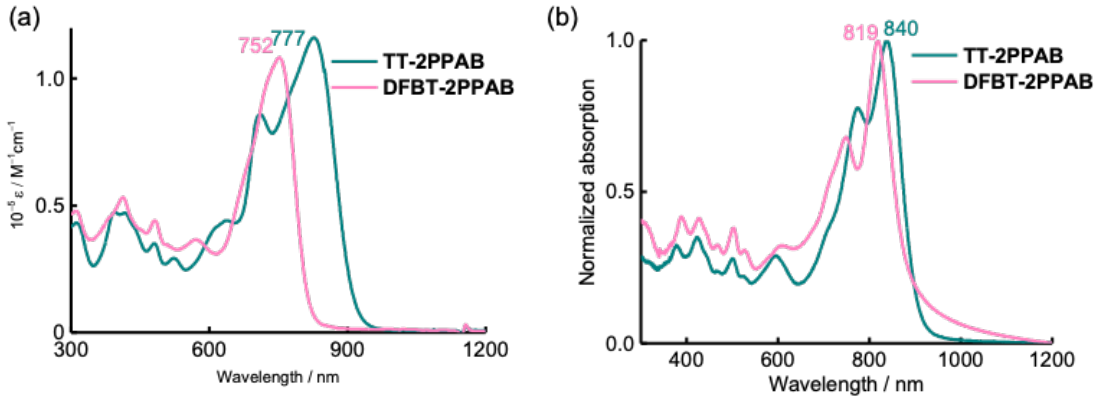

Fig. 1. UV/vis/NIR absorption spectra of **TT-2PPAB** (teal green), and **DFBT-2PPAB** (pink) in (a) chloroform and (b) thin film state.

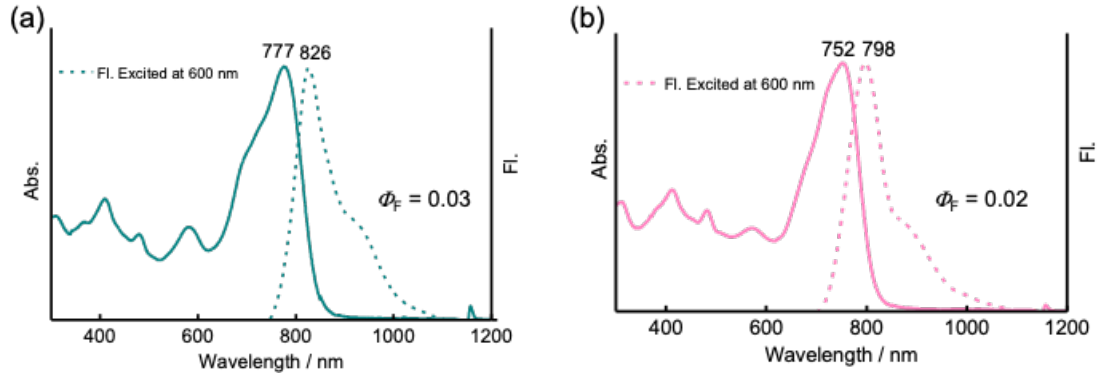

Fig. 2. UV/vis/NIR absorption (solid line) and fluorescence (dashed line) spectra of (a) **TT-2PPAB** and (b) **DFBT-2PPAB** in chloroform.

3.2 Electrochemical properties

Cyclic voltammetry (CV) and differential pulse voltammetry (DPV) measurements were

performed to estimate the redox properties using 0.5 mM sample solutions in dichloromethane containing 0.1 M tetra-*n*-butylammonium hexafluorophosphate as a supporting electrolyte (Fig. 3). Table 1 summarizes the redox potentials and the experimental HOMO and LUMO energy levels determined from the onset of the first oxidation and reduction waves. Similar reduction potentials of **TT-2PPAB** (–1.14 and –1.69 V vs. Fc^+/Fc) and **DFBT-2PPAB** (–1.13 and –1.69 V) indicate the PPAB-centered reductions. Meanwhile, the first oxidation potentials of **TT-2PPAB** and **DFBT-2PPAB** are slightly changed because of the different donor units (0.21 V for **TT-2PPAB**, 0.17 V for **DFBT-2PPAB**). The estimated HOMO energy levels of **TT-2PPAB** and **DFBT-2PPAB** at –4.97 and –4.95 eV, respectively, are deeper than that of **CPDT-2PPAB** at –4.89 eV [32]. This can benefit in enhancing the open-circuit voltage (V_{oc}) values. Estimated electrochemical band gaps are matched well with the trends observed in the optical band gaps.

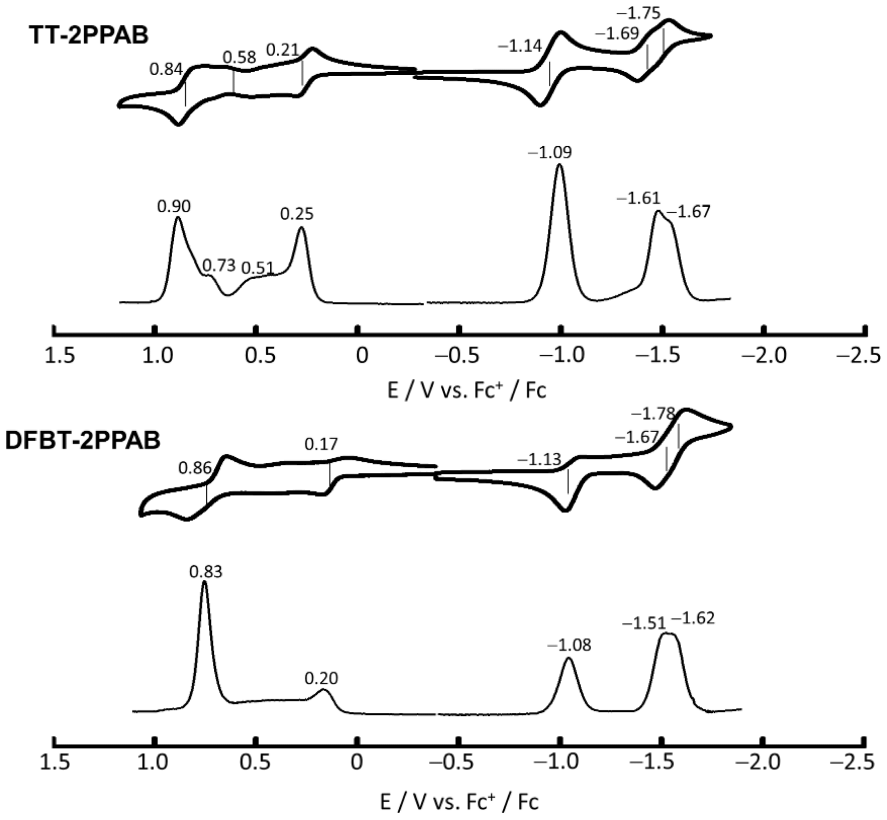

Fig. 3. CV and DPV of **TT-2PPAB** (top) and **DFBT-2PPAB** (bottom) (0.5 mM) in CH_2Cl_2 containing 0.1 M nBu$_4$N·PF$_6$ as a supporting electrolyte (scan rate: 100 mV s^{-1} for CV; pulse amplitude: 0.05 V, pulse width: 0.2 s for DPV).

Table 1. Summary of optical and electrochemical properties of **TT-2PPAB** and **DFBT-2PPAB**.

Compd.	$E_{ox}^{1/2}$ [a] [V]	$E_{red}^{1/2}$ [a] [V]	E_{HOMO} [b] [eV]	E_{LUMO} [c] [eV]	E_g [d] [eV]	λ_{max} [nm]		E_g^{opt} [e] [eV]
						in CH_2Cl_2	in film	
TT-2PPAB	0.21	–1.14	–4.97	–3.74	1.23	777	840	1.35
DFBT-2PPAB	0.17	–1.13	–4.95	–3.71	1.24	752	819	1.38
CPDT-2PPAB[f]	0.10	–1.19	–4.89	–3.68	1.21	827	845	1.30

[a] Determined by CV (conditions: 0.5 mM CH_2Cl_2 solutions containing 0.1 M nBu$_4$N·PF$_6$ as a supporting electrolyte at a scan rate

of 100 mV s^{-1}). Potentials are given relative to the ferrocenium/ferrocene (Fc^+/Fc) couple. [b] $E_{HOMO} = -(E^{ox}_{onset} + 4.8)$ [eV]. [c] $E_{LUMO} = -(E^{red}_{onset} + 4.8)$ [eV]. [d] $E_g = E_{LUMO} - E_{HOMO}$ [eV]. [e] Estimated from film absorption spectra. [f] Data from ref. 32.

3.3 Theoretical calculations

To give an insight into the impact of the donor units on the HOMO energy levels and the band gaps, DFT and TDDFT calculations on the model structures (**TT-2PPAB-c**, and **DFBT-2PPAB-c**), in which alkoxy substituents are replaced with methoxy groups for simplicity, were performed at the CAM-B3LYP/6-31G(d) level (Figs. 4 and S15, and Table S1). The LUMO energy levels are almost similar because the LUMO is mainly localized on the PPAB moiety, whereas the HOMO of **DFBT-2PPAB-c** lies deeper compared with **TT-2PPAB** because of the electron-withdrawing fluorine substituent in the structure of **DFBT**. Despite the slight overestimation, the calculation results reproduce the trend of the HOMO energy levels estimated based on the electrochemical redox potentials. The theoretical absorption spectra of **TT-2PPAB** and **DFBT-2PPAB** are also consistent with the red-shift of the absorption from **DFBT-2PPAB** to **TT-2PPAB** (Table S1).

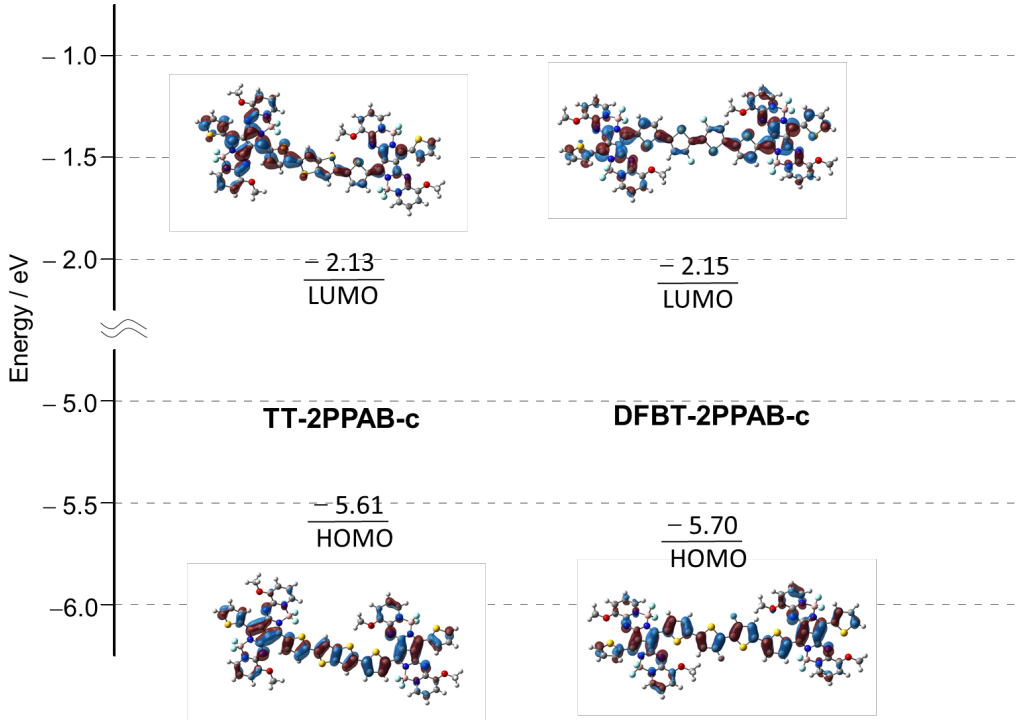

Fig. 4. Frontier molecular orbital diagram of **TT-2PPAB** and **DFBT-2PPAB** (CAM-B3LYP/6-31G(d)).

3.4 Photovoltaic properties

Owing to the shallower LUMO energy levels of **TT-2PPAB** and **DFBT-2PPAB** (–3.71 and –3.74 eV) than that of $PC_{71}BM$ (–4.3 eV), the potential application of **TT-2PPAB** and **DFBT-2PPAB** as p-type OSC materials was examined. Bulk heterojunction-OSCs were fabricated with an inverted device structure of ITO/ZnO (30 nm)/**TT-2PPAB**–**DFBT-2PPAB**:$PC_{71}BM$ (39−121 nm)/MoO_3 (10 nm)/Ag (100 nm) (Fig. 5). The potential device conditions were optimized by controlling triads/$PC_{71}BM$ ratio, amount of additive, and active-layer thickness. As a solvent, chloroform was selected because devices fabricated using chloroform exhibited better performances compared with those prepared using chlorobenzene (Fig. S16 and Table S3). The optimal triad/$PC_{71}BM$ ratio was 1:1 or 1:2 for **TT-2PPAB** (Fig. S17 and Table S4) and 1:1 for **DFBT-2PPAB** (Fig. S23 and Table S10). The device performance was significantly improved using DIO as an

additive (Figs. S18 and S24 and Tables S5 and S11). The optimal volume ratio of DIO was 0.5% both for **TT-2PPAB** (Figs. S19 and S20 and Tables S6 and S7) and **DFBT-2PPAB** (Fig. S25 and Table S12). Finally, the thickness was optimized to 82 nm for **TT-2PPAB** (Figs. S21 and S22 and Tables S8 and S9) and 42 nm for **DFBT-2PPAB** (Fig. S26 and Table S13).

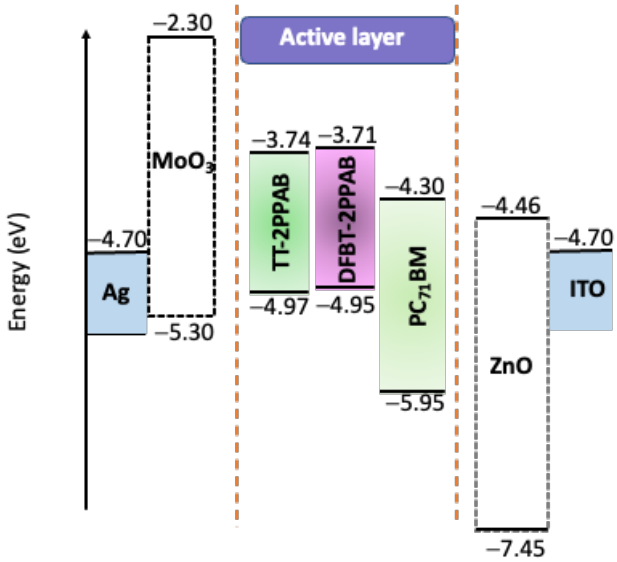

Fig. 5. An inverted device structure of BHJ-OSCs based on **TT-2PPAB**:$PC_{71}BM$ and **DFBT-2PPAB**:$PC_{71}BM$ and the corresponding energy diagram.

Table 2 lists the *J-V* characteristics of the optimized devices. The *J-V* curves and EQE spectra of the **TT-2PPAB**/**DFBT-2PPAB**:$PC_{71}BM$ devices are illustrated in Fig. 6. The **TT-2PPAB**:$PC_{71}BM$ devices achieved a moderately high PCE of 3.11% with J_{sc} of 8.43 mA cm^{-2}, V_{oc} of 0.75 V, and FF of 0.49. As expected, the V_{oc} was improved compared with that of the **CPDT-2PPAB**:$PC_{71}BM$ devices (0.67 V) in our previous study owing to the lower-lying HOMO energy level of **TT-2PPAB**. However, due to the smaller J_{sc} value than **CPDT-2PPAB** (11.7 mA cm^{-2}), the PCE became slightly lower. In contrast to the overall high photovoltaic performance of the **TT-2PPAB**:$PC_{71}BM$ devices, the poor solubility of **DFBT-2PPAB** in chloroform hampered the fabrication of appropriately thick active layers, and the device performance significantly deteriorated. The photoresponse of the **DFBT-2PPAB**:$PC_{71}BM$ devices in the NIR region was lower than that in the visible region probably due to the smaller amount of **DFBT-2PPAB** in the active layer than that expected from the sample concentration. As a consequence, the **DFBT-2PPAB**-based device only gained an inferior PCE of 1.35%.

The EQE spectra of the optimized **TT-2PPAB**:$PC_{71}BM$-based device exhibited reasonable photoresponse in the NIR region (Fig. 6b). The E_{loss} of the **TT-2PPAB**:$PC_{71}BM$-based device is 0.48 eV, which is much smaller than the empirical lower limit of 0.6 eV. Considering that the E_{loss} of the **CPDT-2PPAB**:$PC_{71}BM$-based device in our previous study was similarly low (0.54 eV), PPAB-based triads are highly compatible with $PC_{71}BM$ acceptor. Overall, these results indicate that the PPAB-based SM-OSCs are highly promising in the NIR photovoltaics.

Table 2. Device characteristics of **TT-2PPAB**, **DFBT-2PPAB**, and **CPDT-2PPAB**:$PC_{71}BM$ BHJ-OSCs.

Blend ratio	Solvent and additive[a]	Thickness [nm]	J_{sc} [mA cm^{-2}]	V_{oc} [V]	FF	PCE [%]	E_{loss}[b] [eV]
TT-2PPAB:$PC_{71}BM$ (1:2)	CF:DIO (99.5:0.5 vol%)	82	8.43	0.75	0.49	3.11	0.48
DFBT-2PPAB:$PC_{71}BM$ (1:1)	CF:DIO (99.5:0.5 vol%)	42	3.68	0.69	0.53	1.35	0.55
CPDT-2PPAB:$PC_{71}BM$[c] (1:2)	CF:DIO (99.5:0.5 vol%)	90	11.7	0.67	0.50	3.88	0.54

[a] CF: chloroform, DIO: 1,8-diiodooctane, [b] $E_{loss} = E_g - eV_{oc}$, [c] Data from ref. 32.

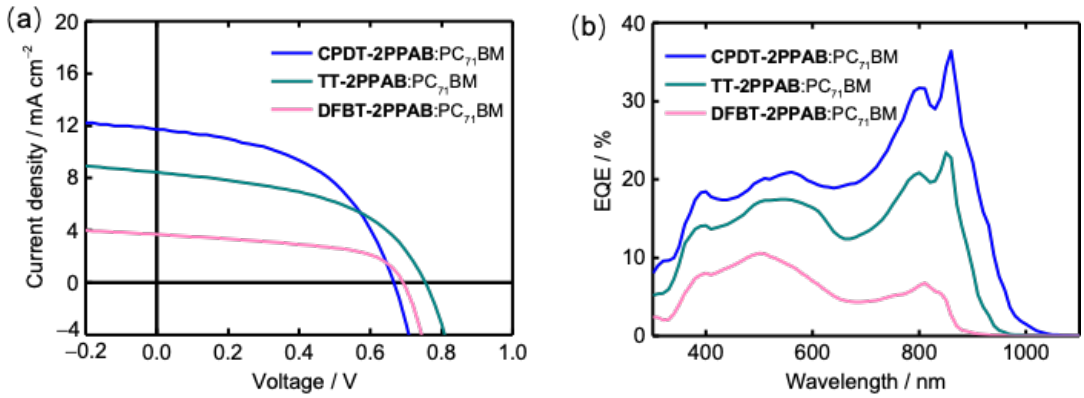

Fig. 6. (a) *J*–*V* curves and (b) EQE spectra of **TT-2PPAB**, **DFBT-2PPAB**, and **CPDT-2PPAB**:$PC_{71}BM$ BHJ-OSCs.

4. Conclusions

In summary, two new PPAB-based A–D–A triads were successfully synthesized, and the donor effect on their absorption spectra and energy levels was investigated. While the LUMOs were dominated by the PPAB as an acceptor unit, the energy levels of HOMOs were significantly stabilized by the donor units. The moderately high PCE of 3.11% with a large V_{oc} of 0.75 V was achieved for the **TT-2PPAB**:$PC_{71}BM$ device owing to the low-lying HOMO of **TT-2PPAB** and small E_{loss}. Although the **DFBT-2PPAB**:$PC_{71}BM$ device exhibited a high V_{oc} of 0.69 V, a small J_{sc} of 3.68 mA cm^{-2} and low NIR photoresponse caused by the poor solubility deteriorated the overall performance. These results demonstrated that V_{oc} can further be improved by modifying the donor units. PPAB-based A–D–A triads in combination with fullerene-based acceptors are highly potential NIR SM-OSC materials because of the high V_{oc} and small E_{loss}. Further investigation to achieve higher OSC performance is intensively investigated in our laboratory and will be reported in due course.

CRediT authorship contribution statement

Ru Feng: Investigation, Visualization, Data curation, Formal analysis, Writing – original

draft. **Tatsuya Mori:** Methodology. **Takuma Yasuda:** Supervision, Methodology. **Hiroyuki Furuta:** Resources, Supervision, Writing-review & editing. **Soji Shimizu:** Funding acquisition, Project administration, Resources, Supervision, Writing-review & editing.

Declaration of competing interest

The authors declare that they have no known competing financial interests or personal relationships that could have appeared to influence the work reported in this paper.

Acknowledgments

This work is supported by Grants-in-Aids from JSPS (No. JP22H02064 and JP19H02703) and Naohiko Fukuoka Memorial Foundation.

Appendix A. Supplementary data

Supplementary data to this article can be found online at https://doi.org/10.1016/j.dyepig.2022.xxxxxx.

References

[1] Inganäs O. Organic Photovoltaics over Three Decades. Adv Mater 2018;30:1–26.

[2] Heeger AJ. 25th anniversary article: Bulk heterojunction solar cells: Understanding the mechanism of operation. Adv Mater 2014;26:10–28.

[3] Lin Y, Li Y, Zhan X. Small molecule semiconductors for high-efficiency organic photovoltaics. Chem Soc Rev 2012;41:4245–72.

[4] Walker B, Kim C, Nguyen TQ. Small molecule solution-processed bulk heterojunction solar cells. Chem Mater 2011;23:470–82.

[5] Mishra A, Bäuerle P. Small molecule organic semiconductors on the move: Promises for future solar energy technology. Angew Chemie Int Ed 2012;51:2020–67.

[6] Collins SD, Ran NA, Heiber MC, Nguyen TQ. Small is Powerful: Recent Progress in Solution-Processed Small Molecule Solar Cells. Adv Energy Mater 2017;7.

[7] Roncali J, Leriche P, Blanchard P. Molecular materials for organic photovoltaics: Small is beautiful. Adv Mater 2014;26:3821–38.

[8] Sun Y, Welch GC, Leong WL, Takacs CJ, Bazan GC, Heeger AJ. Solution-processed small-molecule solar cells with 6.7% efficiency. Nat Mater 2012;11:44–8.

[9] Van Der Poll TS, Love JA, Nguyen TQ, Bazan GC. Non-basic high-performance molecules for solution-processed organic solar cells. Adv Mater 2012;24:3646–9.

[10] Menke SM, Ran NA, Bazan GC, Friend RH. Understanding Energy Loss in Organic Solar Cells: Toward a New Efficiency Regime. Joule 2018;2:25–35.

[11] Veldman D, Meskers SCJ, Janssen RAJ. The energy of charge-transfer states in electron donor-acceptor blends: insight into the energy losses in organic solar cells. Adv Funct Mater

2009;19:1939–48.

[12] Nayak PK, Bisquert J, Cahen D. Assessing possibilities and limits for solar cells. Adv Mater 2011;23:2870–6.

[13] Yang D, Sasabe H, Sano T, Kido J. Low-Band-Gap Small Molecule for Efficient Organic Solar Cells with a Low Energy Loss below 0.6 eV and a High Open-Circuit Voltage of over 0.9 V. ACS Energy Lett 2017;2:2021–5.

[14] Gao K, Li L, Lai T, Xiao L, Huang Y, Huang F, et al. Deep Absorbing Porphyrin Small Molecule for High-Performance Organic Solar Cells with Very Low Energy Losses. J Am Chem Soc 2015;137:7282–5.

[15] Shimizu S. Aza-BODIPY synthesis towards vis/NIR functional chromophores based on a Schiff base forming reaction protocol using lactams and heteroaromatic amines. Chem Commun 2019;55:8722–43.

[16] Shimizu S, Iino T, Araki Y, Kobayashi N. Pyrrolopyrrole aza-BODIPY analogues: A facile synthesis and intense fluorescence. Chem Commun 2013;49:1621–3.

[17] Shimizu S, Iino T, Saeki A, Seki S, Kobayashi N. Rational molecular design towards Vis/NIR absorption and fluorescence by using pyrrolopyrrole aza-BODIPY and its highly conjugated structures for organic photovoltaics. Chem A Eur J 2015;21:2893–904.

[18] Wang L, Xiong Z, Ran X, Tang H, Cao D. Recent advances of NIR dyes of pyrrolopyrrole cyanine and pyrrolopyrrole *aza*-BODIPY: Synthesis and application. Dyes Pigments 2022;198:110040.

[19] Li L, Wang L, Tang H, Cao D. A facile synthesis of novel near-infrared pyrrolopyrrole aza-BODIPY luminogens with aggregation-enhanced emission characteristics. Chem Commun 2017;53:8352–5.

[20] Li W, Wang L, Zhang C, Ran X, Tang H, Cao D. Novel butterfly-shaped AIE-active pyrrolopyrrole aza-BODIPYs: synthesis, bioimaging and diamine/polyamine detection. J Mater Chem C 2022;10:5672–83.

[21] Zhou Y, Ma C, Gao N, Wang Q, Lo PC, Wong KS, et al. Pyrrolopyrrole aza boron dipyrromethene based two-photon fluorescent probes for subcellular imaging. J Mater Chem B 2018;6:5570–81.

[22] Miki K, Enomoto A, Inoue T, Nabeshima T, Saino S, Shimizu S, et al. Polymeric Self-Assemblies with Boron-Containing Near-Infrared Dye Dimers for Photoacoustic Imaging Probes. Biomacromolecules 2017;18:249–56.

[23] Wu C, Huang X, Tang Y, Xiao W, Sun L, Shao J, et al. Pyrrolopyrrole aza-BODIPY near-infrared photosensitizer for dual-mode imaging-guided photothermal cancer therapy. Chem Commun 2019;55:790–3.

[24] Wang L, Xin S, Zhang C, Ran X, Tang H, Cao D. Development of a novel chromophore reaction-based fluorescent probe for biogenic amines detection. J Mater Chem B 2021;9:9383–94.

[25] Li L, Li W, Ran X, Wang L, Tang H, Cao D. A highly efficient, colorimetric and fluorescent probe for recognition of aliphatic primary amines based on a unique cascade chromophore reaction. Chem Commun 2019;55:9789–92.

[26] Li W, Wang L, Sun T, Tang H, Bui B, Cao D, et al. Characterization of nanoparticles combining polyamine detection with photodynamic therapy. Commun Biol 2021;4:1–11.

[27] Wang L, Ran X, Tang H, Cao D. Recent advances on reaction-based amine fluorescent probes. Dyes Pigments 2021;194:109634.

[28] Li L, Li W, Wang L, Tang H, Cao D, Ran X. Pyrrolopyrrole aza-BODIPY dyes for ultrasensitive and highly selective biogenic diamine detection. Sensors Actuators, B Chem 2020;312:127953.

[29] Wang L, Ding H, Tang H, Cao D, Ran X. A novel and efficient chromophore reaction based on a lactam-fused aza-BODIPY for polyamine detection. Anal Chim Acta 2020;1135:38–46.

[30] Ishimatsu R, Shintaku H, Kage Y, Kamioka M, Shimizu S, Nakano K, et al. Efficient Electrogenerated Chemiluminescence of Pyrrolopyrrole Aza-BODIPYs in the Near-Infrared Region with Tripropylamine: Involving Formation of S2 and T2 States. J Am Chem Soc 2019;141:11791–5.

[31] Kage Y, Mori S, Ide M, Saeki A, Furuta H, Shimizu S. Blackening of aza-BODIPY analogues by simple dimerization: Panchromatic absorption of a pyrrolopyrrole aza-BODIPY dimer. Mater Chem Front 2018;2:112–20.

[32] Feng R, Sato N, Yasuda T, Furuta H, Shimizu S. Rational design of pyrrolopyrrole-aza-BODIPY-based acceptor-donor-acceptor triads for organic photovoltaics application. Chem Commun 2020;56:2975–8.

[33] Feng R, Sato N, Nomura M, Saeki A, Nakanotani H, Adachi C, et al. Near-infrared absorbing pyrrolopyrrole aza-BODIPY-based donor-acceptor polymers with reasonable photoresponse. J Mater Chem C 2020;8:8770–6.

[34] Frisch MJ, Trucks GW, Schlegel HB, Scuseria GE, Robb MA, Cheeseman JR, et al. Gaussian 16 Rev. C.01 2016.

[35] Yuan Z, Xiao Y, Yang Y, Xiong T. Soluble ladder conjugated polymer composed of perylenediimides and thieno[3,2-b]thiophene (LCPT): A highly efficient synthesis via photocyclization with the sunlight. Macromolecules 2011;44:1788–91.

[36] Jo JW, Jung JW, Wang HW, Kim P, Russell TP, Jo WH. Fluorination of polythiophene derivatives for high performance organic photovoltaics. Chem Mater 2014;26:4214–20.

[37] Pickett A, Mohapatra A, Laudari A, Khanra S, Ram T, Patil S, et al. Hybrid ZnO-organic semiconductor interfaces in photodetectors: A comparison of two near-infrared donor-acceptor copolymers. Org Electron 2017;45:115–23.